Supplementary Information (SI) for EES Catalysis.

Supplementary Materials for
Are plasmas really catalyst-free?

Thuy Vy Le[1], C. Buddie Mullins[1,2,3], Thomas C. Underwood[3,4]

[1] Department of Chemistry, The University of Texas at Austin, Austin, Texas 78712, United States
[2] McKetta Department of Chemical Engineering, The University of Texas at Austin, Austin, Texas 78712, United States
[3] Texas Materials Institute, The University of Texas at Austin, Austin, Texas 78712, United States
[4] Department of Aerospace Engineering and Engineering Mechanics, The University of Texas at Austin, Austin, Texas 78712, United States
Corresponding author*: thomas.underwood@utexas.edu

The PDF file includes:

Supplementary Text

S1. Materials and Methods

S1.1 Experimental Design:

A nanosecond pulsed spark discharge reactor was built for investigating plasma-assisted ammonia synthesis. The reactor's body was made of high-density polyethylene (HDPE) with a ceramic dielectric center. A quartz window, sealed with an acrylic flange, allowed optical access to the plasma. Electrodes were made from 1/8" diameter Cu, W, or Ni rods (99.99%, McMaster-Carr). The cathode tip was machined to a 45° cone half-angle, while the anode was kept flat. The interelectrode spacing was fixed at 3 mm, and all experiments were conducted at atmospheric pressure. Gas delivery was controlled with calibrated mass flow controllers (MFC): N_2 (99.999%, Airgas, Alicat MC MFC) and H_2 (99.99%, Airgas, Brooks GF40 MFC). The streams were combined downstream of the controllers and homogenized in a stainless-steel static mixer before entering the reactor. The total flow rate varied between 1.2 and 8 sccm, with N_2:H_2 ratios of 1:3 or 1:7. Before plasma ignition, the system was purged with the feed mixture for 15 minutes, and baseline stability was confirmed by GC analysis.

S1.2 Plasma Generation:

Plasma discharges were generated using a high-voltage nanosecond pulser (Airity Technologies, Flare) in conjunction with a waveform generator (SIGLENT SDG1062X) and a DC power supply (Keysight N5752A). Pulses with a duration of 200 ns were applied at a repetition rate of 3 kHz, resulting in an average input power of ~2.5 W. The discharge voltage and current were measured with a high-voltage probe (Tektronix P6015A, 75MHz bandwidth) and a current transformer (Pearson 6585, 250MHz bandwidth), with signals recorded on a digital oscilloscope (Tektronix MSO44). The average discharge energy was ~0.83 mJ/pulse at an applied voltage of around 8 kV. Instantaneous power was calculated by multiplying the voltage and current waveforms, while the energy per pulse was derived by integrating the conduction current across the pulse period. .1.2

S1.3 Analytical Method:

Reactant and product concentrations were quantified using gas chromatography-mass spectrometry (GC–MS, Agilent 8890 GC coupled to a 5977 MSD). The TCD was used specifically for H_2 quantification, as MS detection of H_2 is limited by its small mass and potential interference from the helium carrier gas. The MS was used for quantification of N_2 and NH_3 due to its higher sensitivity and selectivity for these species.Automated sampling was performed through 250 µL gas loops. Permanent gases were separated on a Haysep column connected to the TCD, while a Porabond Q column was employed prior to MS detection. The GC oven was programmed with an initial hold at 60 °C for 2 min, followed by a 100 °C /min ramp to 160 °C, with a final hold of 2 min. Helium was used as the carrier gas at a flow rate of 240mL/min and a split ratio of 400:1.

N_2 and H_2 were calibrated by varying the feed composition, allowing calibration curves to be constructed directly under the same sampling configuration used in the experiments. NH_3 calibration gas (2% in air, CTI) was introduced as the reference standard, with additional dilution in N_2 to provide the desired concentration range. Because NH_3 tends to adsorb strongly on stainless steel walls and valves,[1] the detector response was delayed and unstable until the surfaces were saturated. A long purge time of roughly one hour was required before a steady NH_3 peak could be observed. The transfer line was shortened as much as possible to minimize contact area, but stainless-steel components inside the GC itself could not be eliminated and continued to trap some NH_3. As a result, the NH_3 calibration curve did not pass through the origin but instead showed a non-zero intercept that reflected these systematic adsorption losses (Fig. S2). Together, these calibrations provided a consistent basis for quantifying permanent gases and ammonia products.

S1.4 Surface Characterization:

Scanning Electron Microscopy (SEM) with Energy Dispersive X-Ray Analysis (EDX):

Electrodes were polished prior to operation and subsequently exposed to ~54 million pulses under continuous discharge at 3 kHz and 4 sccm total flow. SEM imaging was performed both before and after plasma exposure using an Everhart–Thornley detector (ETD) at 10 mm working distance, 10 kV accelerating voltage, and 50 pA beam current. All SEM analyses were conducted using a Thermo Apreo 2C field-emission SEM, and EDX spectra were acquired with a Bruker XFlash detector to determine elemental composition. The same SEM/EDX setup was used for both electrode and Si wafer analyses.

Nanoparticles were collected on Si wafers positioned beneath the discharge region. Two discharge energy modes were investigated: low-energy (0.83 mJ/pulse) and high-energy (1.5 mJ/pulse). In both cases, the reaction was exposed to 10^8 pulses at a frequency of 3 kHz, with an average power of approximately 2.5 W and 4.5W respectively, and total flow rate of 4 sccm. SEM imaging of Si-deposited particles was carried out with the ETD detector at 10 mm working distance, 2 kV accelerating voltage, and 1.6 nA beam current.

X-Ray Photoelectron Spectroscopy (XPS):

XPS was performed only on Si wafers that collected plasma-generated nanoparticles. Two sets of samples were analyzed, corresponding to feed gas ratios of N_2:H_2 at 1:3 and 1:7, each exposed to 10^8 pulses at 3 kHz with a total flow of 4 sccm. Measurements were conducted on a VersaProbe 4 instrument equipped with a monochromatic Al Kα source (1486.5 eV). Both survey scans and high-resolution spectra were acquired. Survey scans were collected with a pass energy of 140 eV and step size of 0.5 eV, while high-resolution spectra were acquired at 27 eV pass energy with 0.1 eV step size. Spectra processing was carried out using CasaXPS, and peak fitting utilized both Shirley and Tougaard background corrections, based on the specific region analyzed. Peak envelopes were modeled using Gaussian–Lorentzian (GL30) line shapes, while elemental quantification was conducted with standard relative sensitivity factors.

S1.5 Performance Metrics: The performance of the plasma was characterized by calculating specific energy input (SEI) in eV/molecule,

$$\mathbf{SEI} = \frac{\mathbf{power}}{\mathbf{total\ flow\ rate}},$$

where power is the time-averaged power input to the plasma. The conversion was calculated from inlet and outlet moles as:

$$\mathbf{X} = \frac{\mathbf{n_{before} - n_{after}}}{\mathbf{n_{before}}} * \mathbf{100\%},$$

where n_{before} and n_{after} represent the mole of reactants before and after the plasma discharge. The NH_3 (product) yield was defined relative to the amount of N_2 (reactant) supplied:

$$\mathbf{Y_{NH_3}} = \frac{\mathbf{n_{NH_3}}}{\mathbf{2 * n_{N_2, before}}} * \mathbf{100\%},$$

where $\mathbf{n_{NH_3}}$ is the mole of NH_3 produced through the plasma process.

S.1.6 Error Quantification in Analytical Characterization: Experiments were conducted at least three times to measure random variation (standard deviation) in data.

S2. Publication Datasets

S2.1 Literature Data Mining:

The datasets in Fig. 3 were collected from the Web of Science Core Collection (Clarivate Analytics). All searches used topic fields (TS = title, abstract, author keywords) with Boolean operators**.** The following general conditions were applied across all queries:

Time frame: 1980–2024

Document Type: Article

Language: English

Research Areas: Physics, Chemistry, Materials Science, Engineering, Energy Fuels, Electrochemistry.

Queries used:

(1) Plasma Chemistry: Plasma* AND (reforming OR chemistry OR conversion OR synthesis) NOT (blood OR clinical OR medical OR protein, hemodialysis OR bio* OR patient* OR surgery OR oncolog* OR neur*)

(2) Plasma Catalyst: (1) AND (catalyst OR catalytic OR catalysis)

(3) Plasma not Mention Catalyst: (1) NOT (catalyst OR catalytic OR catalysis)

(4) Plasma Catalytic IB (pack-bed): (2) AND (packed bed OR packed OR packed-bed OR packing discharge OR pellet packed OR bed)

(5) Catalyst-free: (1) AND (catalyst-free OR "catalyst free")

(6) Electrode-Based Plasma without Mentioning Catalysts: (1) AND electrode NOT (catalyst OR catalytic OR catalysis)

S2.2. Unit Conversions from Reported Metrics to SEI and Efficiency Metric:

Literature values of plasma performance are often reported in different forms, including energy yield (g-product/kWh), or SEI in kJ/mol. For consistency in Fig. 3B–C, all data were converted to SEI in eV/molecule. From energy yield,

$$\mathbf{SEI}\left(\frac{\mathbf{eV}}{\mathbf{molecule}}\right) = \frac{\mathbf{2.25*10^{22}*M}}{E_Y*\mathbf{N_A}},$$

Where E_Y is mass of product per electrical energy (g/kWh), M is molar mass of the product (g/mol), N_A is Avogadro number, and relation 1 kWh = $3.6*10^6$ J = $2.25*10^{22}$ eV. From conversion, feed flow, and power:

$$\mathbf{SEI}\left(\frac{\mathbf{eV}}{\mathbf{molecule}}\right)=\frac{\mathbf{P*6.242*10^{18}}}{\mathbf{F*7.45*10^{-7}*X*N_A}},$$

where P is the discharge power (J/s), with 1 J = 6.242*10^{18} eV, F is the mass flow rate of limiting reactant (sccm), with 1sccm = 7.45*10^{-7} mol/s (NIST), X is the reactant conversion (%), and N_A is Avogadro number. From energy cost:

$$\mathbf{SEI}\left(\frac{\mathbf{eV}}{\mathbf{molecule}}\right)=\frac{\mathbf{E*1000*\ 6.242*10^{18}}}{\mathbf{N_A}},$$

where E is the energy cost (kJ/mol), 1 J = 6.242*10^{18} eV, and N_A is Avogadro number.

To compare plasma processes on a consistent basis, conversion efficiency (η_c) and production efficiency (η_f) were used.[2] Conversion efficiency describes how effectively the input electrical energy is stored in the chemical energy of the consumed reactant:

$$\boldsymbol{\eta}_{\mathbf{c}}=\frac{\mathbf{X*|\Delta\hat{H}_r|}}{\mathbf{SEI}},$$

where X is reactant conversion (%), $\Delta\hat{\mathbf{H}}_r$ is the standard reaction enthalpy (eV/molecule), and SEI is specific energy input (eV/molecule). Production efficiency is focused on the formation of a specific product and reflects how much of the supplied energy is captured in that product:

$$\boldsymbol{\eta}_{\mathbf{f}}=\frac{\mathbf{Y*LHV}_{\boldsymbol{product}}}{\mathbf{SEI}},$$

where Y is the product yield relative to the initial reactant (%), $LHV_{product}$ is the lower heat value of the product (eV/molecule).

S2.3. Literature Growth and Supporting CH_4 Data from Literature:

Fig. S1 highlights both the growth of plasma catalysis literature, and the diversity of reactor configurations reported. Panel A shows that while "plasma chemistry" has expanded rapidly since the early 2000s, only a fraction of those studies explicitly mention catalysis, and even fewer focus on packed-bed plasma reactors (catalytic IB). Panel B separates out studies that describe electrodes in direct contact with plasma (catalytic EB) and those claiming "catalyst-free" operation. The latter category has grown steadily, even though electrodes are always present and can introduce catalytic effects. Panel C compiles CH_4 conversion data versus specific energy input from across these different reactor types. The trend shows that catalytic EB[3–6] and catalytic IB[6–15] systems often achieve higher conversions at comparable SEI values than inert EB[8,12,15] cases, indicating that surfaces inside the plasma play a decisive role in determining performance. Together, these datasets illustrate that electrode and boundary interactions should not be overlooked when interpreting plasma catalysis literature.

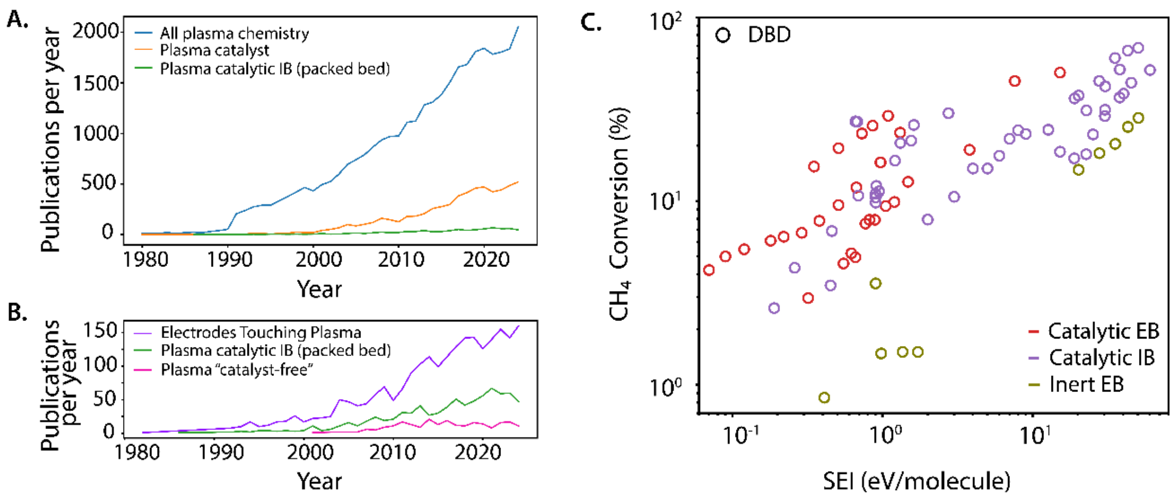

Fig. S1. Literature analysis of plasma catalysis. (A) Annual publications (1980-2024) on plasma chemistry, plasma catalysis, and catalytic IB (packed beds,). (B) Comparison of catalytic IB, catalytic EB, and reports labeled "catalyst-free". (the queries used to generate A-B are detailed in S.2.1) (C) CH_4 conversion vs SEI compiled from literature sources for partial oxidation, grouped by boundary type: inert EB[7,11,14], catalytic EB[2–5], and catalytic IB[5–14].

S3. Gases Quantification and Calibration

Gas-phase species were quantified using gas chromatography–mass spectrometry (GC–MS) with external calibration. Standard gas mixtures were introduced while varying injection volume and composition to establish calibration curves, with the total flow fixed at 8 sccm to match experimental conditions. Detector response (peak area) was plotted against known concentrations. For NH_3, a certified calibration mixture (CTI, 2% NH_3 balance in air) was used, and the same procedure was applied for H_2, N_2, and NH_3 with their respective standards. Calibration factors derived from these curves were applied to all experimental measurements to ensure accurate quantification. N_2 and H_2 calibration ranges encompassed all experimental measurements. For NH_3, experimental measurements ranged from 0.11% to 2.2%; values above ~2% involve minor extrapolation beyond the calibration range.

Systematic Uncertainty from NH_3 Adsorption: The non-zero y-intercept in the NH_3 calibration curve (Fig. S2) introduces a constant systematic offset in concentration determination. From the linear fit ($y = 4087.22x - 71.43$, where y is peak area and x is NH_3 in μmol), the intercept corresponds to an apparent NH_3 amount of approximately 0.017 μmol at zero detector signal. This offset represents ~35% of the lowest measured values (~0.05 μmol) and ~9% of the highest values (~0.2 μmol) within our calibration range. Because this systematic offset is constant across all measurements performed under identical analytical conditions, it does not affect the relative comparisons between electrode materials or feed ratios that form the basis of our conclusions. Readers seeking to make absolute quantitative comparisons should account for this systematic uncertainty of approximately +0.017 μmol.

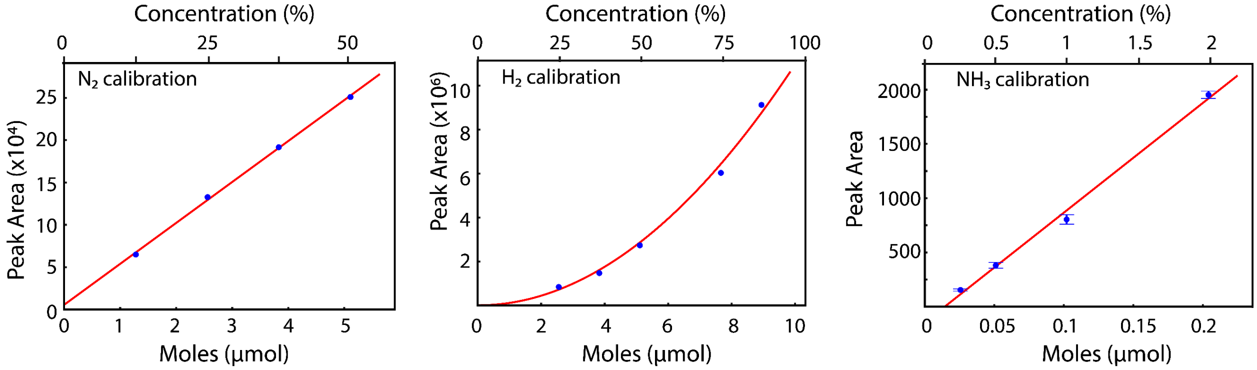

Fig. S2. GC-MS calibration curves for N_2, H_2, and NH_3. Blue markers are experimental data; red lines are fitted curves (linear for N_2 and NH_3, quadratic for H_2). Error bars smaller than the marker size are omitted for clarity.

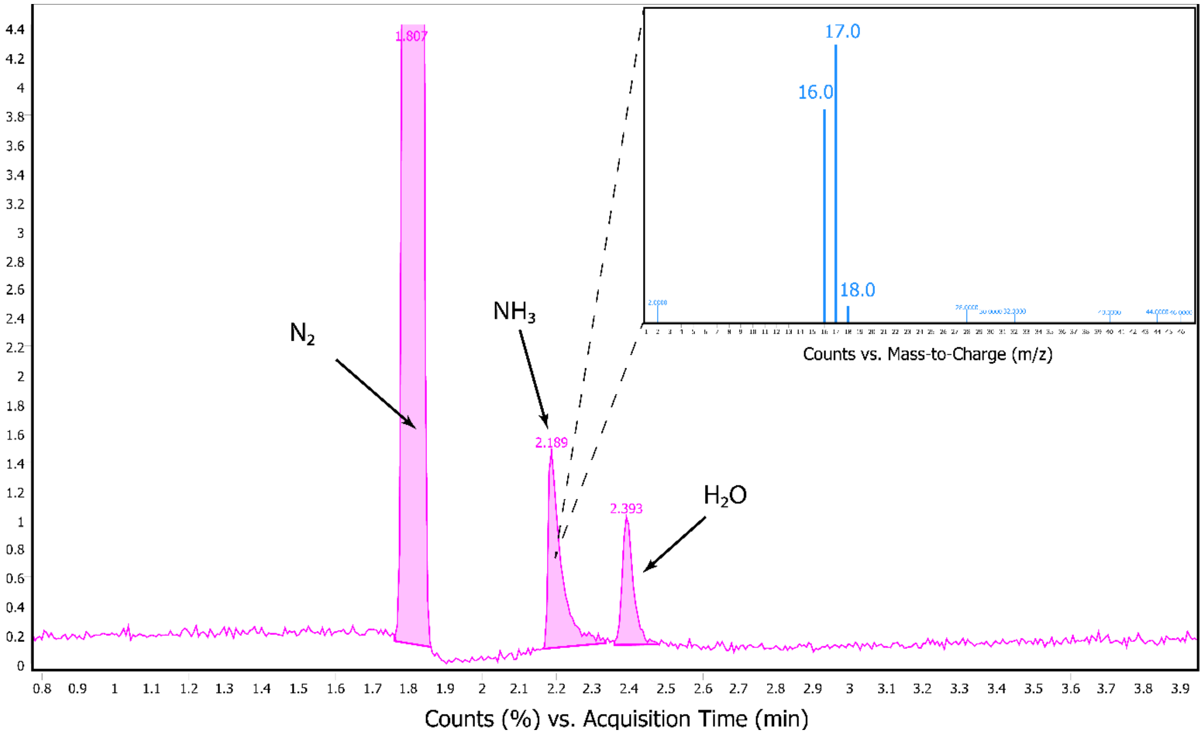

Fig. S3. Representative GC-MS chromatogram for NH_3 calibration. Total ion chromatogram acquired during calibration using a 2% NH_3 standard (balance in air, CTI). Peaks are identified as N_2 (1.807 min), NH_3 (2.189 min), and H_2O (2.393 min). Inset: Mass spectrum of the NH_3 peak showing characteristic electron ionization fragmentation pattern

S4. Plasma Characterization

Voltage and current waveforms were recorded to calculate the energy per pulse. After the trigger (t = 0 ns), the voltage rises to ~8 kV in ~200 ns, while the current presents a narrow ~4 A capacitive spike followed by a small conduction tail that decays to baseline. The pulse energy was calculated by numerically integrating the instantaneous power, $E_p = \int V(t)I(t)dt$, over the pulse window (baseline-subtracted, same probes and sampling as traces).

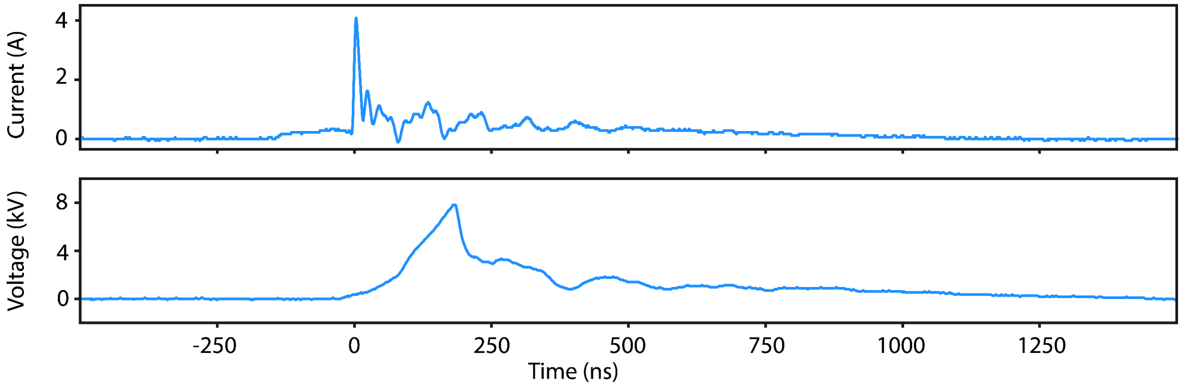

Fig. S4. Recorded current and voltage traces for a single nanosecond discharge pulse.

S5. SEM-EDX Analysis

Particle size distributions were determined from SEM images using ImageJ. Higher magnification images (75,000×) were used for quantification to ensure adequate resolution of individual particles. Images were converted to 8-bit grayscale and binarized using default thresholding. The "Analyze Particles" function was applied to measure particle areas, which were converted to equivalent circular diameters assuming spherical geometry. Particles up to 1000 nm in diameter were included in the analysis.

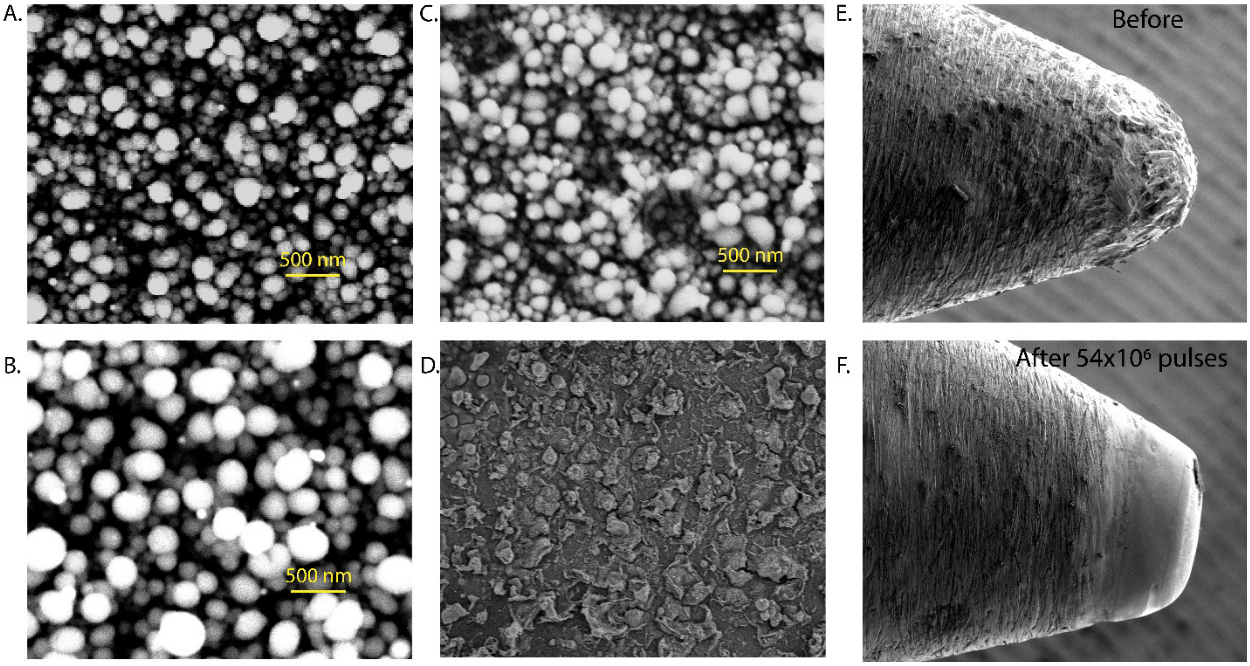

Fig. S5. High magnification SEM characterization of plasma generated nanoparticles and electrode erosion. (A) Nanoparticles collected on Si wafer at 0.83 mJ/pulse energy (10^8 pulses, N_2:H_2 = 1:3, 4 sccm) (B) Nanoparticles collected at 1.5 mJ/pulse energy under identical conditions (C) Nanoparticles collected at 0.83 mJ/pulse with doubled exposure time (2×10^8 pulses), demonstrating that total accumulated energy increases particle density but does not reproduce the larger particle sizes observed at higher instantaneous pulse power. (D) Higher-magnification image of the spark-active zone on the flat anode electrode (corresponding to the orange region in Fig. 6C), revealing micro-melt pool morphology with smooth resolidified surfaces and surrounding ejected debris. (E-F) Pointed cathode tip electrode before (E) and after (F) 54×10^6 pulses, showing pronounced erosion and surface roughening consistent with concentrated electric field enhancement and intense ion bombardment from the cathode fall region.

S6. XPS Analysis

Wide surveys (0–1200 eV) and high-resolution scans of C 1s, O 1s, N 1s, Cu 2p, and Cu LMM were collected in the same session to minimize drift. To rectify the charge, the adventitious C 1s peak was fixed at 284.8 eV, and a Shirley background was applied to all areas. Peaks were fitted with Voigt line forms (GL (30)), with widths restricted to related components and placements maintained within expected chemical ranges. C 1s was defined by C-C/C-H at 284.8eV, C-O at 285.6 eV, and O-C=O at 288.8 eV. O 1s included lattice oxygen on Cu at 530.4 eV, hydroxide/adsorbed oxygen at 531.8eV, oxygen in Al_2O_3 at 531.1eV, and oxygen from the Si wafer at 532.8eV. The Cu $L_3M_{45}M_{45}$ envelope was deconvoluted into state-specific multiples with seven peaks for Cu^0, four for Cu^+, and four for $Cu2^+$; internal spacings, intensities, and widths were fixed to reference values, while only a global shift, width scaling, and amplitudes were refined.[16] Auger peaks were analyzed in kinetic energy rather than binding energy, since Auger transitions have well-defined KE values independent of X-ray energy, and reference values for Cu oxidation states are tabulated in KE; this also retains the validity of the modified Auger parameter. After assigning the oxidation state from the Cu-$L_3M_{45}M_{45}$ fit, the Cu 2p3/2 binding energy was determined from the modified Auger parameter,

$$\alpha' = \mathrm{BE}\ (\mathrm{Cu2p}_{3/2}) + \mathrm{KE}\ (\mathrm{Cu}\ L_3M_{45}M_{45}),$$

using reference α′ values from Cu (1851.32 eV), Cu_2O (1849.4 eV), and CuO (1891.9 eV).[17] Identical fitting limits and parameters were used across all samples, with typical uncertainties of ~0.05–0.10 eV in peak positions.

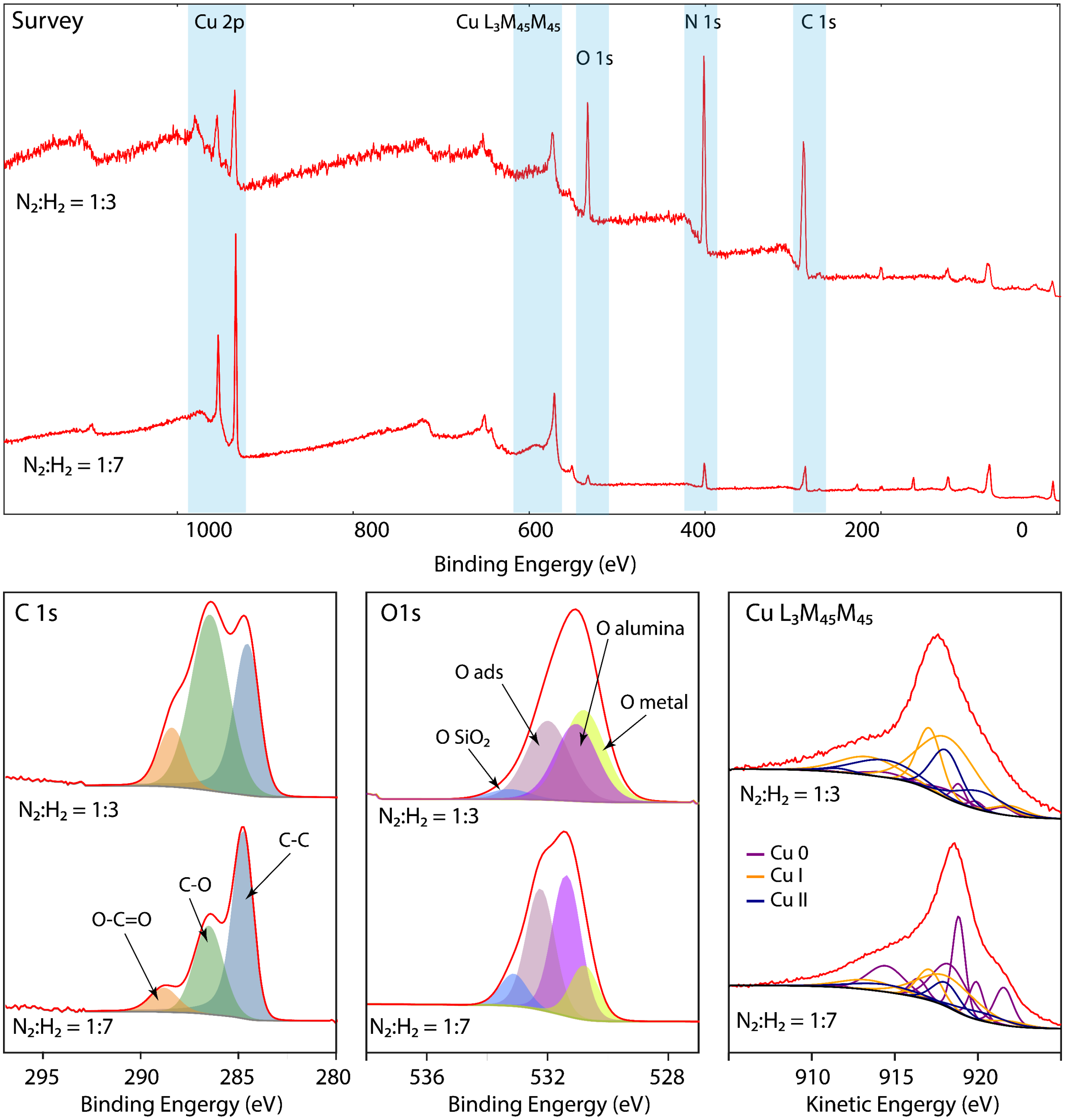

Fig. S6. Survey and high-resolution XPS of plasma-generated nanoparticles on Si wafer at different feed gas composition. The top panel shows survey spectra for samples, the bottom panels display the corresponding high-resolution fits of C 1s, O 1s and the Cu $L_3M_{45}M_{45}$ Auger envelope.

References

1 O. Vaittinen, M. Metsälä, S. Persijn, M. Vainio and L. Halonen, Adsorption of ammonia on treated stainless steel and polymer surfaces, *Appl. Phys. B*, 2014, **115**, 185–196.

2 C. R. Nallapareddy and T. C. Underwood, What is "efficiency" in plasma chemical processes?, *iScience*, 2025, **28**, 112297.

3 T. Nozaki, A. Hattori and K. Okazaki, Partial oxidation of methane using a microscale non-equilibrium plasma reactor, *Catalysis Today*, 2004, **98**, 607–616.

4 M. Okumoto and A. Mizuno, Conversion of methane for higher hydrocarbon fuel synthesis using pulsed discharge plasma method, *Catalysis Today*, 2001, **71**, 211–217.

5 X. Zhang and M. S. Cha, Partial oxidation of methane in a temperature-controlled dielectric barrier discharge reactor, *Proceedings of the Combustion Institute*, 2015, **35**, 3447–3454.

6 H. Lee and D. H. Kim, Direct methanol synthesis from methane in a plasma-catalyst hybrid system at low temperature using metal oxide-coated glass beads, *Sci Rep*, 2018, **8**, 9956.

7 L. Chen, X.-W. Zhang, L. Huang and L.-C. Lei, Partial oxidation of methane with air for methanol production in a post-plasma catalytic system, *Chemical Engineering and Processing: Process Intensification*, 2009, **48**, 1333–1340.

8 P. Chawdhury, Y. Wang, D. Ray, S. Mathieu, N. Wang, J. Harding, F. Bin, X. Tu and Ch. Subrahmanyam, A promising plasma-catalytic approach towards single-step methane conversion to oxygenates at room temperature, *Applied Catalysis B: Environmental*, 2021, **284**, 119735.

9 D. Lašič Jurković, H. Puliyalil, A. Pohar and B. Likozar, Plasma-activated methane partial oxidation reaction to oxygenate platform chemicals over Fe, Mo, Pd and zeolite catalysts, *Int J Energy Res*, 2019, er.4806.

10 B. Pietruszka, K. Anklam and M. Heintze, Plasma-assisted partial oxidation of methane to synthesis gas in a dielectric barrier discharge, *Applied Catalysis A: General*, 2004, **261**, 19–24.

11 M. Shareei, H. Taghvaei, A. Azimi, A. Shahbazi and M. Mirzaei, Catalytic DBD plasma reactor for low temperature partial oxidation of methane: Maximization of synthesis gas and minimization of CO2, *International Journal of Hydrogen Energy*, 2019, **44**, 31873–31883.

12 L. Song, Y. Kong and X. Li, Hydrogen production from partial oxidation of methane over dielectric barrier discharge plasma and NiO/γ-Al2O3 catalyst, *International Journal of Hydrogen Energy*, 2017, **42**, 19869–19876.

13 A. Indarto, H. Lee, J.-W. Choi and H. K. Song, Partial Oxidation of Methane with Yttria-stabilized Zirconia Catalyst in a Dielectric Barrier Discharge, *Energy Sources, Part A: Recovery, Utilization, and Environmental Effects*, 2008, **30**, 1628–1636.

14 T. Jiang, Y. Li, C. Liu, G. Xu, B. Eliasson and B. Xue, Plasma methane conversion using dielectric-barrier discharges with zeolite A, *Catalysis Today*, 2002, **72**, 229–235.

15 F. De Rosa, C. Hardacre, W. G. Graham, G. McCullough, P. Millington, P. Hinde and A. Goguet, Comparison between the thermal and plasma (NTP) assisted palladium catalyzed oxidation of CH4 using AC or nanopulse power supply, *Catalysis Today*, 2022, **384–386**, 177–186.

16 M. C. Biesinger, Advanced analysis of copper X-ray photoelectron spectra, *Surface & Interface Analysis*, 2017, **49**, 1325–1334.

17 C. D. Wagner, The NIST X-ray photoelectron spectroscopy (XPS) database.